Lab on a Chip

PAPER

View Article Online
View Journal | View Issue

Cite this: *Lab Chip*, 2026, **26**, 954

Surface modification of 3D printed microfluidic devices by photochemical grafting

Guohao Yang,[a] Seonghun Shin,[a] Seongsu Cho,[b] Jinkee Lee *[ac] and Ryungeun Song *[d]

Received 24th October 2025,
Accepted 23rd January 2026

DOI: 10.1039/d5lc00994d

rsc.li/loc

Three-dimensional (3D) printing has emerged as a promising method for fabricating microfluidic devices due to its rapid prototyping, adaptability, and cost-effectiveness. However, the intrinsic hydrophobicity of commercial photocurable resins limits their ability to generate stable oil-in-water (O/W) emulsion droplets. In this study, we addressed this limitation by introducing a simple yet effective surface modification technique, photochemical grafting, which covalently attaches hydrophilic methacrylic acid groups onto the surfaces of 3D-printed channels, enabling reliable monodisperse O/W droplet formation. Integrating two modules with contrasting wettabilities yields a modular platform for single-step production of double emulsions (W/O/W and O/W/O). The result is a versatile system with precise control over droplet formation and exceptional monodispersity with tunable shell-to-core ratios. The grafted surfaces retained wettability and droplet-generation performance after three months of storage and 25 hours of continuous shear. Collectively, this work presents a robust and scalable strategy to bridge rapid 3D printing with durable surface functionalization, expanding the potential of customizable emulsion generation in lab-on-a-chip applications.

1. Introduction

Emulsions are stable mixtures of two immiscible liquids, typically oil and water, in which droplets of one liquid (the dispersed phase) are surrounded by the other (the continuous phase). They possess unique physicochemical properties that make them valuable across many industries. For example, in the pharmaceutical industry, emulsions improve drug delivery and bioavailability.[1–3] In the cosmetic industry, they enhance texture and stability of products,[4,5] and in the food industry, they contribute to desirable texture and shelf life.[6–8] Emulsions are also used for controlled release of pesticides in agriculture[9] and in the production of advanced composite materials in materials science.[10,11] Over the past few decades, microfluidic technology has enabled the preparation of highly monodisperse emulsions with precise control over droplet size, which is essential for applications that require consistent performance. Various fabrication methods have been developed to fabricate microfluidic devices, each with its own benefits and drawbacks. Capillary glass-based systems, for instance, are easy to fabricate and offer excellent optical transparency, but these systems require manual alignment during assembly, which often leads to poor reproducibility and inconsistent droplet generation.[12–15] Soft lithography using polydimethylsiloxane (PDMS) is widely employed due to its low cost, high flexibility, and excellent biocompatibility.[16–18] However, PDMS has high permeability to gases and vapors and a low elastic modulus (0.5 to 4 MPa), rendering it susceptible to pressure-induced deformation and therefore unsuitable for long-term or high-pressure applications.[19–21] Conventional glass microfluidics fabricated through wet etching[22] provides superior chemical resistance and mechanical stability. However, the fabrication process is costly and time-consuming, and requires cleanroom facilities, which limits both accessibility and scalability. Furthermore, a critical challenge across these conventional platforms is the difficulty of achieving spatially localized wettability control, which is essential for generating complex fluids such as double emulsions. Achieving distinct wettability patterns within a channel typically necessitates labor-intensive masking steps[23,24] or precise flow treatments,[25–27] significantly increasing fabrication complexity and hindering mass production.

In recent years, three-dimensional (3D) printing has emerged as a promising alternative for microfluidic device

[a] *School of Mechanical Engineering, Sungkyunkwan University, Suwon, 16419, Republic of Korea. E-mail: lee.jinkee@skku.edu*
[b] *Department of Chemical and Biomolecular Engineering, School of Engineering and Applied Science, University of Pennsylvania, Philadelphia, Pennsylvania 19104, USA*
[c] *Institute of Quantum Biophysics, Sungkyunkwan University, Suwon, 16419, Republic of Korea*
[d] *School of Mechanical Engineering, Chungbuk National University, Cheongju, 28644, Republic of Korea. E-mail: rsong@chungbuk.ac.kr*

fabrication, offering rapid design iteration, complex 3D geometries, and low-cost prototyping without the need for specialized infrastructure.[28,29] The employment of polymeric 3D printing materials also demonstrates considerable potential for on-demand emulsion generation.[30–32] Still, the generation of oil droplets within a continuous water phase remains challenging.[33] This difficulty arises primarily from the fact that commercial photocurable resins typically exhibit a higher affinity for oil than for water, causing the oil to spread along the channel walls rather than forming stable oil-in-water (O/W) emulsion droplets inside 3D-printed microfluidic channels. In contrast to the well-established surface modification strategies for PDMS, the functionalization of 3D-printed materials, particularly commercial resins with undisclosed chemical compositions, remains a relatively underdeveloped field. Plasma treatment, such as oxygen plasma,[34] has been demonstrated to enhance hydrophilicity in a temporary manner. However, these effects are known to dissipate over time due to molecular rearrangement or degradation of surface groups. Hwang *et al.* employed a silica nanoparticle coating technique to render the printed surface hydrophilic.[35] Although this method improves wettability, the physical surface adsorption-based coating is prone to detachment at high flow rates, limiting its suitability for applications requiring long-term stability. Yoon *et al.* employed an organic–inorganic hybrid resin (HP resin) as the channel material, which possesses intrinsic hydrophilicity; however, the fabrication process requires photolithographic equipment, thereby increasing the overall cost.[36] Männel *et al.* developed intrinsically hydrophilic 3D printing resins;[37] nevertheless, this approach limits accessibility for commercial 3D printers and may compromise critical properties such as mechanical strength and printing resolution. Alternatively, Bacha *et al.* applied a photochemical grafting method to convert 3D-printed droplet generator surfaces from a hydrophobic to a hydrophilic state.[38] Despite these efforts, the open-channel configuration adapted in that study introduced several drawbacks. In particular, oxygen inhibition reduces the effectiveness of surface grafting, and the open structure may cause leakage during droplet generation.

This study addresses the inherent limitations of hydrophobic, closed-channel 3D-printed microfluidic devices by photochemically grafting hydrophilic functional groups onto the internal channel surface, thereby enabling the stable generation of O/W emulsion droplets. Furthermore, by integrating two microfluidic devices with distinct surface wettabilities, we demonstrate the successful formation of both oil-in-water-in-oil (O/W/O) and water-in-oil-in-water (W/O/W) double emulsion droplets. The surface modification is achieved through ultraviolet (UV)-induced grafting of methacrylic acid, using benzophenone as a photo-initiator to activate the reaction under UV exposure.[39] This process effectively alters the channel surface from hydrophobic to hydrophilic, promoting the reliable formation of oil droplets in aqueous environments. Notably, the grafting method is highly efficient even within enclosed microchannels, due to the reduced oxygen inhibition in such confined geometries.[40] In addition, this technique is time efficient, forming a thin polymeric layer without compromising the dimensional fidelity or structural integrity of the 3D-printed structures.[41] As a result, this method preserves both the performance and resolution of the device while enabling reproducible and stable emulsification. Moreover, the modular implementation of this technique facilitates spatially selective wettability control through simple assembly, circumventing the complex masking steps required in conventional monolithic devices. Combined with the capability for simultaneous batch treatment, this photochemical grafting strategy offers a practical and scalable solution for advanced emulsion generation in 3D-printed microfluidic systems.

2. Experimental

2.1 Materials

Sorbitan monooleate (Span 80), polysorbate 20 (Tween 20), *n*-hexadecane (99%), deionized water (DI-water), methacrylic acid (99%), benzophenone, castor oil and polyvinyl alcohol (PVA, molecular weight 13–23 kDa) were purchased from Sigma Aldrich Co. (USA). Ethanol (94.5%) was purchased from Samchun Pure Chemicals (Republic of Korea).

2.2 Fabrication of 3D-printed microfluidic devices

The microfluidic devices were designed using 3D computer aided design (CAD) software (SolidWorks, Dassault Systems) to define precise geometries and internal features. The resulting 3D modeling files were transferred to a high-resolution, multi-jet 3D printer (Projet MJP 2500 Plus, 3D Systems) for fabrication. The printer employed a transparent, UV-curable resin (VisiJet M2R-CL) and a wax material (VisiJet M2 SUP) to fabricate the primary material and the sacrificial structure, respectively. This material combination ensured optical transparency of the devices for visualization and allowed the printing of complex microchannel structures. Subsequently, the printed devices underwent post-processing to remove the sacrificial wax material, followed by cleaning procedures to attain smooth channel surfaces and transparency. After printing, the modules were placed in a convection oven at 80 °C to melt the wax layers. Once fully melted, the residual wax was initially removed using a hot oil bath, followed by ultrasonication in a detergent-containing water bath. To eliminate any remaining detergent, the modules were subsequently rinsed by ultrasonication in deionized water. Each cleaning step was performed for a minimum of 30 minutes.[28]

In this study, three types of microfluidic devices were designed for distinct purposes. Device type I (Fig. 1a) was developed for measuring contact angles, which serve as a crucial parameter for evaluating surface wettability and interfacial affinity. Another device, type II (Fig. 1b), was fabricated to generate single emulsion droplets using a planar flow-focusing geometry, where the dispersed phase is

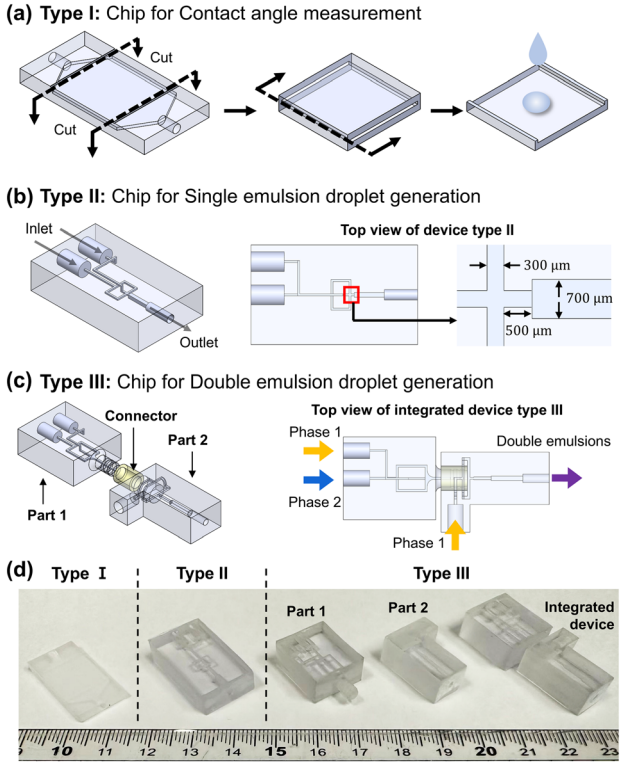

Fig. 1 Design and schematic of 3D-printed microfluidic devices. (a) Type I: device designed for contact angle measurement, showing the cutting process to measure channel wettability. (b) Type II: device for single emulsion droplet generation, including a schematic of the channel geometry and the top-view layout with channel dimensions. (c) Type III: device for double emulsion droplet generation, composed of parts 1 and 2 connected *via* a connector. The top-view schematic illustrates the integrated configuration and flow paths of phases 1 and 2 leading to double emulsion formation. (d) Photographs of the 3D-printed microfluidic devices corresponding to type I, II, and III designs.

injected perpendicularly into the continuous phase. This configuration is widely employed in microfluidic research owing to its ease of fabrication and scalability for large-scale production.[42,43] The third device (Fig. 1c) was designed for generating double-emulsion droplets through the integration of two microfluidic modules with distinct wettability characteristics, which were connected *via* a press-fit connector to ensure robust integration and prevent leakage. Fig. 1d presents photographs of the 3D-printed devices corresponding to each design and their assembled configuration.

2.3 Droplet generation procedure

The droplet generation experiments were conducted using the 3D printed microfluidic devices described in the previous section. The water and oil phases were introduced into the device through syringe pumps (PHD Ultra Advanced Syringe Pump, Harvard Apparatus), enabling precise control over the flow rates of the dispersed and continuous phases. Typical flow rates ranged from 10 to 400 μl min^{-1}, depending on the desired droplet size. The droplet generation process within the microfluidic channel was monitored in real time using a high-speed camera (FastCam Mini 100, Photron) mounted on an optical microscope (U-LH100-3, Olympus Corporation). The camera operated at 2000 fps, providing sufficient temporal resolution to capture the dynamics of droplet formation. Microscopy images were recorded at a high resolution of 4 μm per pixel to clearly visualize the smallest droplets and flow characteristics within the microchannels. Subsequent to the acquisition of the images, the data were analyzed manually using PFV4 software (Photron).

To evaluate the performance of droplet generators, both single and double emulsion droplets (*e.g.*, O/W, W/O, O/W/O, and W/O/W) were produced by varying the flow configuration and the surface wettability of the devices. Additional details on device combinations and flow parameters are summarized in section 3.

2.4 Procedure of photochemical grafting

The photochemical grafting procedure was adapted from the mechanism proposed by Tretinnikov *et al.*, in which benzophenone acts as a photo-initiator.[44] Upon UV exposure (~254 nm wavelength), benzophenone absorbs energy and abstracts hydrogen atoms from the polymer surface, generating surface-bound macroradicals. These radicals initiate the grafting of methacrylic acid monomers, forming a covalently bonded hydrophilic layer. It is assumed that all reactions occur in an environment lacking in oxygen, given that oxygen has a significant inhibitory effect on the progress of the grafting reactions.[45]

The grafting solution was prepared by dissolving 2 M methacrylic acid and 12 mM benzophenone in 10% (v/v) ethanol in DI-water. The solution was magnetically stirred and purged with nitrogen gas for 30 minutes prior to use to remove dissolved oxygen and prevent interference with the grafting reaction. During the deoxidation step, no appreciable reduction in the solution volume was observed. For surface modification, the 3D-printed microfluidic devices were placed in a polystyrene Petri dish. The grafting solution was then introduced into the channels using a pipette to ensure full coverage. The devices were then completely submerged in the solution so that the solution level exceeded the top surface of the device by approximately 5 mm. The Petri dish was immediately covered with a polystyrene lid to minimize ambient oxygen exposure. The entire process, from solution injection to covering, was completed within one minute. UV irradiation was performed using a mercury UV lamp (light source of MDA-400M, Midas System, 16.5 mW cm^{-2} at 365 nm wavelength). The 20 minute UV exposure of the devices activated the benzophenone and grafted methacrylic acid on the microchannel surfaces, resulting in hydrophilic surfaces. When higher UV intensity is used, shorter exposure time is sufficient, though excessive exposure can lead to undesirable over-polymerization or degradation. After UV treatment, the microfluidic devices were thoroughly rinsed with DI-water to

remove any unreacted monomer and photo-initiator, thereby ensuring that only the grafted polymer remains on the device surface. Subsequently, the devices were air-dried at room temperature, allowing any residual moisture to evaporate, thus preparing the device for subsequent use in experiments. This controlled grafting procedure provides a reliable method to ensure consistent surface modification across multiple microfluidic devices.

2.5 Measuring surface characteristics

To evaluate surface wettability, water contact angles were measured *via* the sessile drop method with a drop shape analyzer (DSA 100, KRÜSS GmbH). A 4 μL droplet of DI-water was automatically dispensed onto the 3D-printed surfaces to ensure precision and consistency. Measurements were performed 30 seconds after droplet deposition to allow stabilization, thereby providing an accurate assessment of the surface hydrophilicity. Contact angle values were quantified using ADVANCE software (KRÜSS GmbH). For each surface type, measurements were conducted on at least three independently prepared samples, with three measurements performed at different positions on each sample. The measured contact angles were averaged to evaluate the uniformity and reproducibility of the photochemical grafting.

The surface morphology was characterized using scanning electron microscopy (SEM; JSM-7600F, JEOL Ltd.). Prior to imaging, each sample was coated with a thin layer of platinum/gold (~20 nm) using a sputter coater (208 High Resolution Sputter Coater, Ted Pella) to enhance image contrast and clearly visualize fine surface features. Chemical modification of the surfaces was analyzed by Fourier transform infrared (FTIR) spectroscopy (I2001, Midac Corporation). Spectra were obtained for both grafted and unmodified samples to identify the functional groups introduced by the photochemical grafting process.

3. Results and discussion

3.1 Droplet generation without photochemical grafting

As illustrated in Fig. 2a and b, W/O emulsion droplets were successfully generated within a 3D-printed microfluidic channel. In this configuration, the dispersed phase (d) was DI-water with 1% (v/v) Tween 20, and the continuous phase (c) was *n*-hexadecane with 1% (v/v) Span 80. Due to the nonpolar nature of the 3D-printed polymer, the hydrophobic channel surface exhibits higher affinity toward the non-polar oil phase than the polar water phase. As a result, the oil preferentially wets the channel surface, while the water phase remains suspended, enabling stable droplet formation. The compatibility between the oil and the hydrophobic channel surface is crucial for maintaining the W/O emulsion droplets. The results in Fig. 2b demonstrate that stable droplet generation is maintained across a wide range of flow rate (Q) conditions. The blue-colored regions in the images were

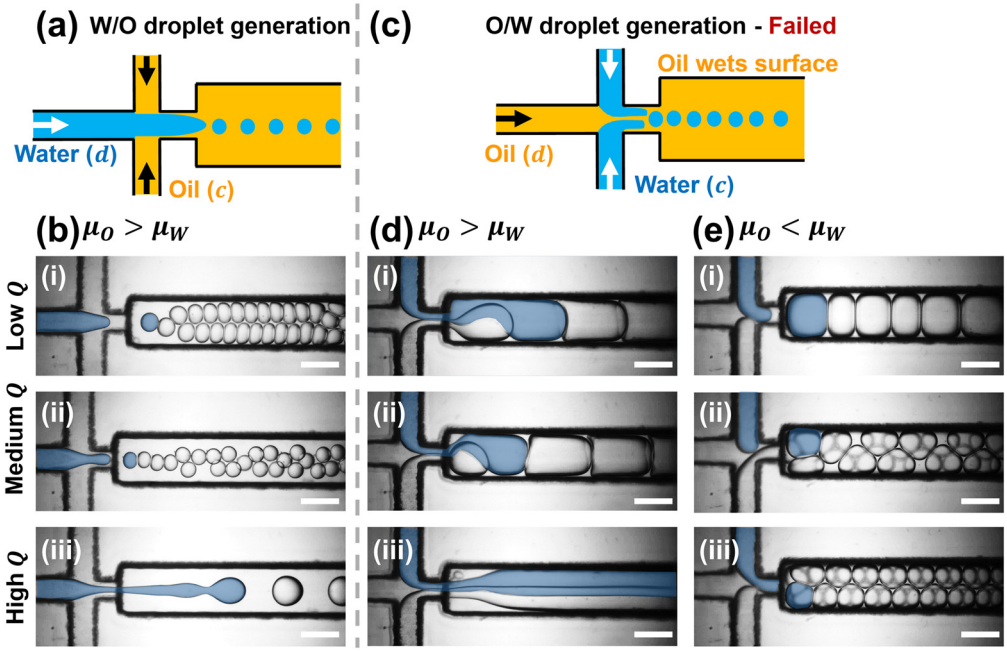

Fig. 2 Single emulsion droplet generation without photochemical grafting. (a) Schematic of successful water-in-oil (W/O) droplet generation. (b) Microscopy images of W/O droplet formation within a 3D printed channel at varying flow rates (Q). The blue-colored regions in the images were artificially highlighted through image processing to emphasize the moment of first droplet formation. (c) Schematic diagram of failed oil-in-water (O/W) droplet generation due to surface wettability; oil preferentially wets the channel surface. Experimental results for O/W droplet generation with different continuous phases: (d) water with 1% (v/v) Tween 20 (low viscosity); (e) 6% (w/v) PVA (high viscosity). The dispersed phase is *n*-hexadecane with 1% (v/v) Span 80 in both cases. Scale bars represent 600 μm. Flow conditions are (i) low Q: Q_C = 40 μL min^{-1}, Q_d = 10 μL min^{-1}; (ii) medium Q: Q_C = 200 μL min^{-1}, Q_d = 50 μL min^{-1}; (iii) high Q: Q_C = 400 μL min^{-1}, Q_d = 100 μL min^{-1}.

Table 1 Flow conditions and corresponding droplet generation regimes

Flow conditions	Q_c/Q_d (μL min^{-1})	Regime	Droplet size (μm)	Generation frequency (Hz)
Low	40/10	Dripping	~300	Low (9.41)
Medium	200/50	Dripping	~250	High (84.9)
High	400/100	Jetting	~500	Medium (23.8)

artificially highlighted through image processing to emphasize the moment of first droplet formation. Table 1 summarizes the droplet formation characteristics under different flow conditions while maintaining a constant flow rate ratio (Q_c/Q_d = 4). Despite these variations, droplet formation remained stable under all conditions, indicating robust performance of the 3D-printed device in the W/O emulsion droplet generation.

In contrast, as shown in Fig. 2c, generating O/W emulsion droplets proved to be challenging under the same device. When water was used as the continuous phase and oil as the dispersed phase, stable O/W emulsion droplet formation was not achieved. This instability arises because the non-polar oil phase preferentially wets the hydrophobic 3D-printed channel surface, rather than remaining suspended within the polar water phase. As a result, the oil adheres to the channel walls, disrupting the breakup process and inhibiting the formation of discrete droplets. This wetting behavior ultimately causes a phase inversion, where the oil becomes the continuous phase and water becomes the dispersed phase, regardless of the intended configuration. These observations highlight the critical influence of surface wettability in determining the success or failure of droplet generation in multiphase microfluidic systems.

To further explore this effect, Fig. 2d presents results obtained under the same flow conditions used for W/O droplet generation. Here, the water phase colored similarly to Fig. 2b, intended as the continuous phase, unexpectedly breaks into droplets, confirming the reversal of the emulsion structure. To counteract this undesired phase behavior, the viscosity of the continuous phase (μ_c) was increased above that of the dispersed phase (μ_d) by using 6% (w/v) PVA solution, as shown in Fig. 2e. The higher viscosity ($\mu_o < \mu_c$) was expected to suppress discretization of the water phase and promote O/W droplet formation. However, even under these modified conditions, the system continued to favor W/O emulsification. These results further validate that surface wettability, rather than the flow regime or viscosity, is the dominant determinant of emulsion behavior in 3D-printed channels.

3.2 Surface modification *via* photochemical grafting

The experimental steps of the UV grafting process, as described previously, are illustrated in Fig. 3a. The unmodified 3D-printed polymer surface has an inherent hydrophobic nature, as evidenced by the contact angle of 103.23° ± 5.41° (Fig. 3b(i)). This high contact angle indicates

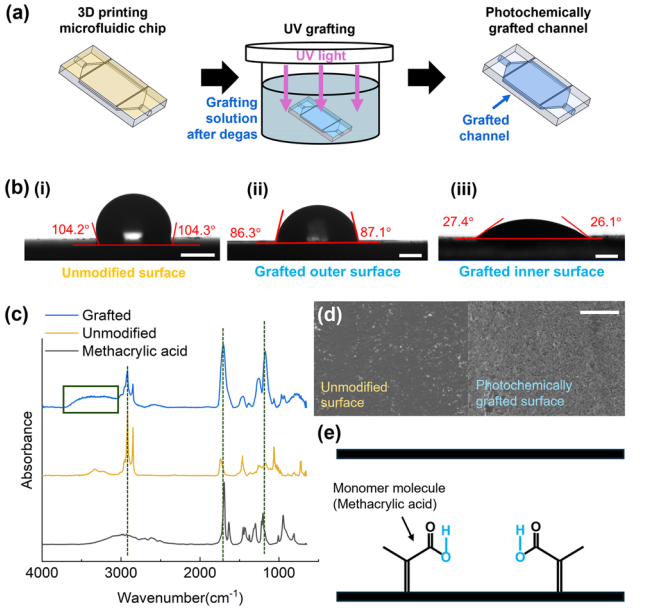

Fig. 3 Surface modification *via* photochemical grafting. (a) Schematic of the photochemical grafting process applied to a 3D-printed microfluidic device. (b) Contact angle measurements on different surfaces: (i) unmodified 3D-printed surface. (ii) Outer surface of the 3D-printed chip after photochemical grafting. (iii) Inner surface after photochemical grafting. The scale bars represent 1 mm. (c) FTIR spectra of the unmodified 3D-printed material, the photochemically grafted surface, and the methacrylic acid monomer used for graft modification. (d) SEM images of the unmodified and photochemically grafted surfaces of a 3D-printed part. The scale bar represents 100 μm. (e) Illustration of the photochemical grafting mechanism. Methacrylic acid monomers form hydrogen bonds with the 3D-printed surface, leading to surface functionalization and enhanced hydrophilicity.

a low affinity for water. Following the photochemical grafting process, contact angles were measured on both the outer surface (Fig. 3b(ii)) and the inner surface after the grafting (Fig. 3b(iii)) of the 3D-printed device to evaluate the effectiveness of surface modification. While the outer surface showed a slight decrease in contact angle, the inner surface exhibited a significant reduction to 29.27° ± 2.39°, reflecting a pronounced transition to a hydrophilic state. This enhanced hydrophilicity can be ascribed to the reduced oxygen inhibition within enclosed channels. This method exhibits high efficiency when the thickness of the monomer solution layer is on the order of a few hundred micrometers. Due to the limited thickness of the monomer solution layer and the absence of atmospheric oxygen inflow, the dissolved oxygen initially present in the monomer solution is rapidly consumed through photooxidation reactions occurring at the substrate polymer surface. Consequently, the residual molecular oxygen exerts only a negligible influence on the efficiency of grafting polymerization.[46]

The presence of hydrophilic methacrylic acid groups on the grafted polymer surface was confirmed by Fourier transform infrared spectroscopy (FTIR) analysis, as shown in Fig. 3c. The FTIR spectrum of the grafted surface exhibited characteristic peaks corresponding to newly introduced

functional groups. In particular, a strong peak observed at approximately 1700 cm^{-1} is attributed to the C=O stretching vibration of carbonyl groups derived from methacrylic acid. A peak at 1250 cm^{-1} corresponds to C–O bonds, while a broad peak spanning 3200–3600 cm^{-1} (marked with a rectangle) indicates the presence of hydroxyl (O–H) groups. These peaks were either absent or significantly weaker in the spectrum of the unmodified surface, thereby validating the successful attachment of methacrylic acid and the formation of hydrophilic functional groups in the polymer process. In addition to the emergence of hydrophilic peaks, a reduction in peak intensity at near 3000 cm^{-1}, corresponding to C–H bonds, was also observed after the grafting process. This reduction is attributed to the photoinitiated grafting mechanism, in which benzophenone abstracts hydrogen atoms from the polymer backbone under UV irradiation, creating reactive sites for monomer attachment. The resulting decrease in C–H bonds reflects a subtle modification of the base chemical structure of the polymer.

Scanning electron microscopy (SEM) was employed to examine the surface morphology before and after the photochemical grafting process. As shown in Fig. 3d, the pristine 3D-printed surface exhibited a smooth and homogeneous texture, reflecting the intrinsic characteristics of the printed polymer. After grafting, the surface appeared more heterogeneous, with fine irregular features observed across the substrate. These morphological differences are indicative of the formation of a grafted polymeric layer.[38] Although SEM imaging provides only qualitative insight into surface topography, the observed contrast between the pristine and grafted surfaces supports the FTIR results, confirming that the photochemical process induced both chemical modification and noticeable alteration in surface texture.[47]

These chemical and morphological changes are directly linked to the enhanced hydrophilicity of the grafted surface. As illustrated in Fig. 3e, the methacrylic acid monomers are covalently grafted onto the 3D-printed surface through the photochemical grafting mechanism, introducing polar functional groups such as hydroxyl (–OH). This incorporation of polar moieties transforms the originally non-polar hydrophobic polymer surface into a polar hydrophilic one.[48] As a result, the modified surface exhibits a stronger affinity toward water than oil, allowing the water phase to act as the continuous phase during droplet generation. This transition is crucial for achieving stable O/W emulsions in 3D-printed microfluidic devices. Given that the benzophenone-initiated grafting mechanism relies on C–H bonds ubiquitous in commercial photocurable resins (*e.g.*, acrylates and methacrylates), this technique offers broad compatibility with various 3D printing materials. We empirically validated this versatility by successfully applying the method to a different commercial 3D printing resin (VisiJet M2S-HT90), confirming that the approach is adaptable to a wide range of materials used in additive manufacturing.

3.3 Droplet generation after photochemical grafting

Following surface modification *via* photochemical grafting, the stable generation of O/W emulsion droplets became feasible, in contrast to the unsuccessful attempts observed prior to surface treatment. The hydrophilic inner channel surface enabled water to serve as the continuous phase and oil as the dispersed phase, allowing for controlled droplet formation across a wide range of flow conditions. The dispersed phase consisted of *n*-hexadecane with 1% (v/v)

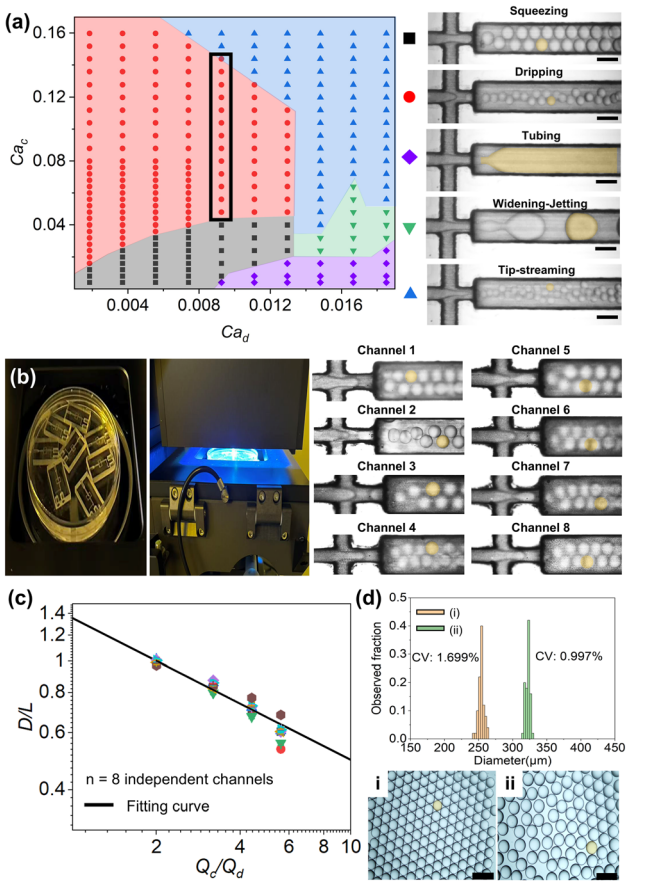

Fig. 4 Single emulsion droplet generation *via* the photochemically grafted device. (a) Regime map of O/W emulsion droplet formation in 3D-printed microfluidic devices after photochemical grafting, plotted as a function of the capillary numbers of the continuous phase (Ca_c) and dispersed phase (Ca_d). Different regimes are visualized by microscopy images: squeezing, dripping, extended droplet, widening-jetting and tip-streaming. Scale bars are 600 μm. (b) Demonstration of batch processing capability. Photographs of the experimental setup for simultaneous UV grafting of eight devices in a single Petri dish, and microscopy images showing stable O/W emulsion droplet generation in all eight independently treated channels (channels 1 to 8). (c) Evaluation of device-to-device reproducibility. Plot of normalized droplet size (D/L) and flow rate ratio (Q_c/Q_d) measured from eight independently grafted devices (channels 1 to 8) processed in a single Petri dish. The solid line represents the power-law fitting curve ($D/L = 1.36(Q_c/Q_d)^{-0.44}$), corresponding to the region highlighted in (a). (d) Size distribution and optical images of monodispersed O/W emulsion droplets collected in a Petri dish. (i) Q_c = 100 μL min^{-1}, Q_d = 50 μL min^{-1}. (ii) Q_c = 200 μL min^{-1}, Q_d = 50 μL min^{-1}. The scale bars represent 600 μm.

Span 80, introduced at flow rates ranging from 10 to 100 μL min^{-1}. The continuous phase was 6% (w/v) PVA aqueous solution, with flow rates between 10 and 400 μL min^{-1}. Under these conditions, five distinct droplet generation regimes were observed, as shown in the regime map according to the regimes of squeezing, dripping, tubing, widening-jetting and tip-streaming shown in Fig. 4a.[13,49,50] The classification of regimes is based on the capillary number (Ca), a dimensionless parameter defined as $Ca = \mu U/\gamma$, where μ is the dynamic viscosity, U is the flow velocity, and γ is the interfacial tension between the two fluids. The Ca quantifies the relative influence of viscous forces on interfacial tension, determining the mode of droplet formation in multiphase flow systems.

In the squeezing regime (black squares), which occurs at low Ca values for both the continuous (Ca_c) and dispersed (Ca_d) phases, the dispersed phase obstructs the junction, forming droplets larger than the channel dimensions. As Ca_c increases, the system transitions into the dripping regime (red circles), characterized by droplet pinch-off at the nozzle of the dispersed phase. In this mode, the droplet size becomes smaller than the channel width. When Ca_d is high and Ca_c remains low, the tubing regime (purple diamond) emerges, where interfacial tension dominates and droplet breakup is suppressed within the observation window. As Ca_c increases, the system transforms into the widening-jetting regime (green inverted triangles), in which an elongated liquid jet breaks into droplets downstream *via* Rayleigh–Plateau instability. Finally, as Ca_c continues to increase, the system enters a tip-streaming regime (blue triangles). Under extensional or shear flow, an isolated droplet was deformed into a pointed-tip morphology, and the tips served as sites where slender jets or minute daughter droplets were emitted.

To validate the scalability and device-to-device reproducibility of the proposed method, eight droplet generators were treated simultaneously in a single Petri dish and quantitatively evaluated under the dripping regime, whose theoretical behavior is well characterized, to confirm its consistency with conventional droplet generation systems. The Q_d was fixed at 50 μL min^{-1} while the Q_c was varied from 100 to 280 μL min^{-1}. As shown in Fig. 4b, the experimental data from all eight independently grafted channels exhibit a highly consistent trend in which increasing the Q_c leads to a reduction in droplet diameter (D), attributed to the enhanced viscous shear stress acting on the interface, which promotes faster necking and pinch-off of the dispersed phase. This behavior aligns with the scaling laws $D/L = b(Q_c/Q_d)^a$,[51] where L is the channel width and a and b are empirical constants. In this study, the fitted relation yielded $D/L = 1.36(Q_c/Q_d)^{-0.44}$, indicating strong agreement with theoretical predictions and demonstrating the tunability of droplet size through flow rate control. The data points are tightly clustered around the fitting curve, indicating minimal device-to-device variation. This confirms that the batch photochemical grafting process yields uniform surface wettability across multiple chips. PVA contained in the continuous phase effectively suppresses coalescence and aggregation, allowing droplets generated in the 3D-printed device to be collected in a Petri dish. The comparative images in Fig. 4c confirm that droplet size can be precisely tuned by adjusting the flow rates of both phases. The resulting droplets exhibited excellent monodispersity, with a coefficient of variation (CV) of around 1–2%. It is worth noting that the diameter of the collected droplets appears slightly larger than that observed in the microchannel. Because during droplet generation, insufficient surfactant coverage at the neck leads to a high interfacial tension and thus a smaller initial droplet size.[51] Subsequent surfactant adsorption lowers the interfacial tension and Laplace pressure, allowing the droplet to slightly expand and reach a relaxed equilibrium shape. Consequently, droplets collected in the Petri dish appear larger than those formed inside the microchannel.[52]

3.4 Double emulsion generation

The successful generation of double emulsions was achieved by sequentially integrating two 3D-printed microfluidic modules with contrasting surface wettabilities. One module was rendered hydrophilic *via* photochemical grafting, while the other retained its native hydrophobicity. This modular design enabled precise control over phase interfaces at each emulsification stage, facilitating the formation of both W/O/W and O/W/O emulsion droplets. For instance, an inner oil phase first emulsified within an aqueous phase using a hydrophilic module. The resulting coaxial jet was then introduced into a hydrophobic module, where it was sheared into droplets by the outer oil phase. This process generated O/W/O emulsion droplets, each consisting of an oil core encapsulated by an aqueous shell and suspended in the outer oil phase (Fig. 5a). Reversing the wettability of the two modules enabled the formation of W/O/W emulsion droplets (Fig. 5b).

Fig. 5c and d demonstrate the controlled generation of both W/O/W and O/W/O double emulsion droplets using the integrated devices previously illustrated in Fig. 5a and b, respectively. For both configurations, the output from the first module seamlessly enters the second module without observable disturbance, confirming the effective hydraulic integration of the hydrophilic and hydrophobic units. In the first module, a coaxial jet was formed, enabling the generation of double emulsion droplets in a single step. The inner and middle phases were either a 10% (w/v) PVA solution with 1% (v/v) Tween 20 or castor oil containing 1% (v/v) Span 80. The outer phase consisted of 10% (w/v) PVA solution for W/O/W emulsion droplets or castor oil without a surfactant for O/W/O double emulsion droplets. The exclusion of a surfactant from the outer phase was essential, since excessively low interfacial tension between the outer and middle phases prevents droplet breakup and instead stabilizes a coaxial jet. The compositions and key physical parameters of each configuration are summarized in Table 2.

In the case of W/O/W double emulsion generation, droplets were formed in the dripping regime (Fig. 5c). In this

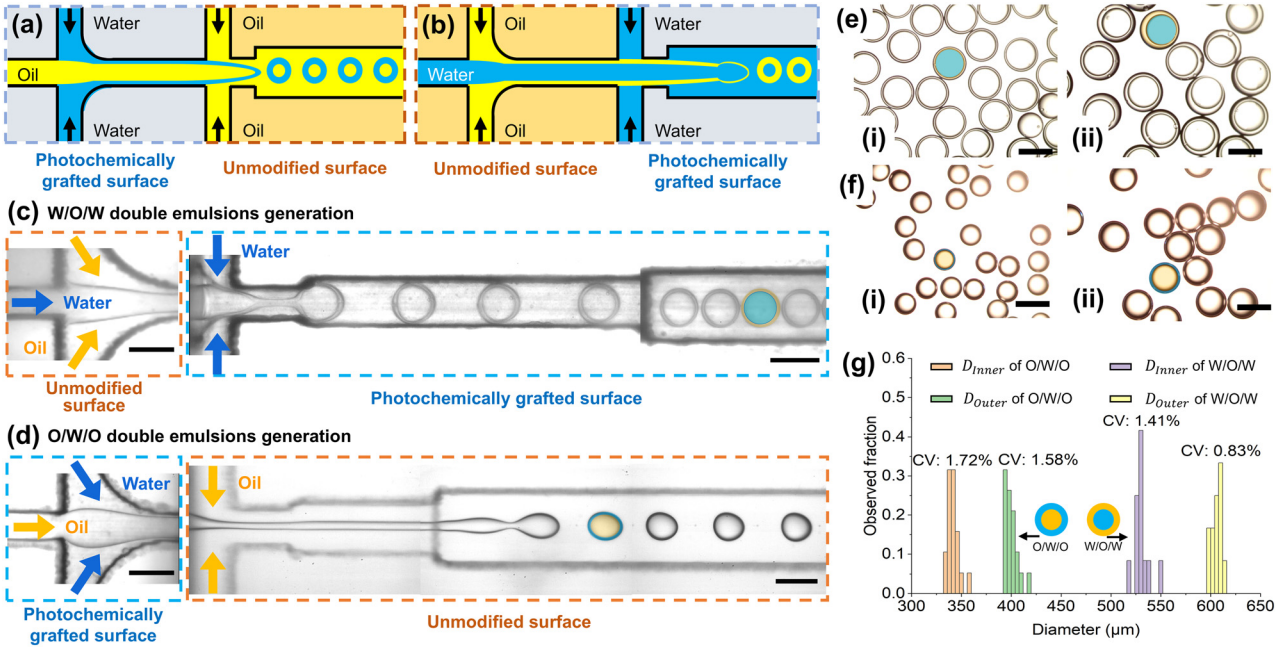

Fig. 5 Generation of double emulsion droplets *via* sequentially integrated 3D-printed microfluidic modules. (a) Schematic picture of O/W/O droplet generation. (b) Schematic picture of W/O/W droplet generation. (c) Formation of W/O/W droplets using a two-stage microfluidic system: the unmodified surface generates the water core, followed by oil shell encapsulation through the channel with the photochemically grafted surface. (d) Formation of O/W/O droplets using the same system with a reversed surface configuration: the photochemically grafted surface generates the oil core, and the unmodified surface facilitates water shell formation. (e) Collected W/O/W double emulsions under two different flow conditions: (i) Q_i = 10 μL min^{-1}, Q_m = 8 μL min^{-1}, Q_o = 50 μL min^{-1}; (ii) Q_i = 10 μL min^{-1}, Q_m = 14 μL min^{-1}, Q_o = 50 μL min^{-1}. (f) Collected O/W/O double emulsions under two different flow conditions: (i) Q_i = 10 μL min^{-1}, Q_m = 5 μL min^{-1}, Q_o = 50 μL min^{-1}; (ii) Q_i = 10 μL min^{-1}, Q_m = 13 μL min^{-1}, Q_o = 50 μL min^{-1}. The scale bars represent 600 μm. (g) Size distribution of the collected double emulsions shown in (c) and (d), indicating high monodispersity.

Table 2 Key physical parameters for double emulsion generation

Type	Phase	Solution	Interfacial tension (mN m^{-1})	Viscosity (mPa s)
O/W/O emulsion	Inner phase	Castor oil + 1% Span 80	—	650
	Middle phase	DI water + 10% PVA + 1% Tween 20	1.6	80
	Outer phase	Castor oil		650
W/O/W emulsion	Inner phase	DI water + 10% PVA + 1% Tween 20	—	80
	Middle phase	Castor oil + 1% Span 80	3.4	650
	Outer phase	DI water + 10% PVA		80

state, a bulbous end developed at the tip of the coaxial fluid, and its interfacial area gradually expanded as the inner and middle phases were continuously injected. As the inner fluid drained through the narrowing neck, the fluid stream at the neck eventually pinched off, producing a single droplet encapsulated within the middle-phase bulbous end. The trailing filament was immediately retracted by interfacial tension. Subsequently, the bulbous end of the middle phase pinched off under the combined effect of interfacial tension and viscous drag exerted by the outer phase, resulting in the formation of a W/O/W double emulsion droplet containing a single inner aqueous core. In contrast, O/W/O double emulsion generation occurred predominantly in the jetting regime (Fig. 5d). In this case, a long coaxial jet was observed between the fluid inlets and the droplet formation site, which constitutes the primary distinction from the dripping mode. Due to the high velocity of the outer phase, the viscous drag acting on the middle and inner fluids increased substantially, giving rise to a highly elongated fluid stream at the neck covered by the middle phase. Unlike the dripping mode, no bulbous end formed near the neck, as both the middle and inner fluids were advected downstream by the large viscous drag imposed by the continuous outer flow.

The difference between the W/O/W and O/W/O formation modes can be attributed to both the viscosity of the outer phase and the interfacial tension between the outer and middle phases.[14] In the case of W/O/W emulsions, the relatively higher interfacial tension between the outer and middle phases results in a lower capillary number, favoring the dripping regime. By contrast, in the O/W/O configuration,

the interfacial tension is substantially reduced due to the presence of a surfactant in the outer aqueous phase, which increases the capillary number and promotes jetting by suppressing the retraction of the compound jet. In addition, the viscosity of the outer phase plays a crucial role. The much higher viscosity of the oil phase in the O/W/O configuration enhances the viscous stress acting on the interface, leading to pronounced stretching of both the inner and middle jets. Consequently, the combination of a lower interfacial tension and a more viscous outer phase in the O/W/O system results in a higher capillary number and a stable jetting mode.

The tunability of the droplet morphology was further demonstrated in the W/O/W system by varying the flow rate of the middle oil phase while maintaining constant inner and outer aqueous-phase flow rates. As shown in Fig. 5e(i) and (ii), increasing the oil-phase flow rate led to a gradual thickening of the shell, indicating that the shell thickness can be effectively modulated by adjusting the flow rate of the middle phase. This trend reflects the dynamic balance between viscous drag and interfacial tension at the inner oil–water interface, offering a robust means to customize the internal structure of W/O/W droplets. By contrast, such control was less effective in the O/W/O configuration, where the aqueous shell thickness remained nearly constant despite variations in the middle-phase flow rate (Fig. 5f(i) and (ii)). This insensitivity may stem from interfacial hysteresis or delayed interface deformation under high-viscosity outer-phase conditions. As a result, the shell exhibits limited adaptability, constraining the extent of morphological tuning achievable in the O/W/O regime.

Finally, both double emulsion configurations demonstrated excellent monodispersity, as confirmed by droplet size distributions in Fig. 5g. Importantly, the size of the double emulsions is primarily governed by the dimensions of the printed channel rather than the surface modification process itself. Since photochemical grafting operates at the molecular level, it is not limited by geometric constraints. Therefore, with the adoption of higher-resolution 3D printing technologies capable of fabricating finer channels, this technique can be readily extended to produce double emulsions down to the scale of tens of micrometers. These results underscore the effectiveness of the proposed dual-module design in generating customizable, high-quality double emulsions using 3D-printed microfluidic platforms.

3.5 Durability of photochemical grafting

In order to ensure the long-term usability of the photochemically treated 3D-printed microfluidic device, its static and dynamic durability properties were examined separately. Fig. 6a shows the results of static durability testing. The microfluidic device was hermetically sealed and stored in a Petri dish for three months. To monitor possible temporal variations, the contact angle between water and the 3D-printed surface was measured daily during the first seven days after grafting and once again after three months of storage. Throughout this period, the contact angle remained nearly constant, showing 27.92° ± 4.65° after three months, which is not significantly different from that of the freshly grafted surface. This result indicates that the surface wettability remains stable over time following photochemical grafting.

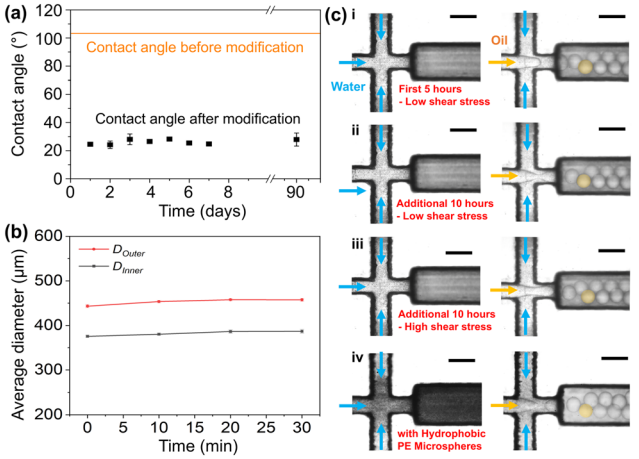

Fig. 6 Stability and durability assessment of the photochemically grafted surface. (a) Static durability test showing time-dependent contact angle between water and the 3D-printed surface after photochemical grafting. For the results on days 1, 4, 5, 6, and 7, the error is within 5% of the mean value and is therefore not visible in the figure. (b) Temporal stability of double emulsion generation. Time-dependent variation of the average diameter (D_{Outer} and D_{Inner}) over 30 minutes of continuous operation, demonstrating consistent droplet size. (c) Dynamic durability testing. Microscopy images of stable oil droplet generation after being subjected to various stress conditions: (i) after 5 hours of continuous phase flushing at 100 μL min^{-1}; (ii) after an additional 10 more hours of continuous phase flushing at 100 μL min^{-1}; (iii) after an additional 10 hours of continuous phase flushing at 500 μL min^{-1}; (iv) after 4 hours of flushing with an aqueous suspension containing 10 μm hydrophobic PE microspheres. Scale bars represent 600 μm.

We also evaluated the temporal stability of the grafted surface during the generation of complex fluids. As shown in Fig. 6b, we monitored the average diameters of O/W/O double emulsion droplets (D_{Inner} and D_{Outer}) over a continuous 30 minute operation. The results showed negligible fluctuation in droplet size throughout the process, confirming that the device maintains a steady state and precise wettability control without temporal drift.

After assessing static durability, we further evaluated the dynamic stability of the grafted surface. First, a continuous aqueous phase was flowed through the channel at a low flow rate of 100 μL min^{-1}, corresponding to an estimated wall shear stress of 0.56 Pa given the 300 μm channel width. Stable O/W droplet generation was maintained after 5 hours of continuous operation (Fig. 6c(i)). The same flow conditions were maintained for an additional 10 hours (total 15 hours), during which no change in droplet formation behavior was observed (Fig. 6c(ii)), indicating preserved surface functionality. Subsequently, the flow rate was increased to 500 μL min^{-1}, corresponding to a shear stress of

approximately 2.8 Pa. Even after another 10 hours of continuous flow at this higher shear rate (Fig. 6c(iii)), the droplet generation remained stable. These results confirm that the grafted surface maintains its wetting properties under prolonged shear exposure across a wide range of hydrodynamic conditions. To further assess the mechanical robustness and fouling resistance, we conducted an accelerated scratch test using a suspension of hydrophobic fluorescent polyethylene (PE) microspheres (10 μm diameter). The particle-laden aqueous phase was flushed through the microchannel at 200 μL min^{-1} for 4 hours. Crucially, given the hydrophobic nature of the microspheres, any coating failure or exposed hydrophobic patches would typically lead to particle adhesion and aggregation *via* hydrophobic interactions. However, as shown in Fig. 6c(iv), no particle accumulation or fouling was observed on the channel walls even after prolonged contact. This absence of aggregation not only confirms the mechanical stability of the grafted layer against abrasion but also verifies the uniformity of the hydrophilic modification, effectively preventing non-specific hydrophobic adsorption.

4. Conclusions

In this work, we successfully applied and validated a photochemical grafting approach to overcome the intrinsic hydrophobicity of 3D-printed microfluidic devices. By grafting methacrylic acid functional groups onto the internal channel surfaces, the devices were converted to a hydrophilic state, enabling stable O/W emulsion droplet generation that has previously been challenging in 3D-printed systems. The modified surfaces demonstrated excellent tunability of droplet size across multiple flow regimes, with high monodispersity and reproducibility. Moreover, by integrating modules with contrasting surface wettabilities, we achieved reliable formation of both W/O/W and O/W/O double emulsions, providing precise control over the internal morphology and shell thickness. These results highlight the versatility of the proposed method in advancing emulsion-based applications such as drug delivery, biomolecular encapsulation, and diagnostic assays.

Durability tests further confirmed the long-term stability of the grafted surfaces, with wettability and droplet generation performance maintained after three months of storage and extended operation under shear flow. This robustness underscores the practicality of photochemical grafting for real-world applications, bridging the gap between rapid 3D printing and durable functionalization.

It is worth noting that while photolithographic methods offer superior spatial resolution for intricate micron-scale patterning, our approach prioritizes practical applicability through a modular design. By circumventing the complexity of internal alignment and masking, this study establishes a practical and scalable pathway to engineer long-lasting, functional 3D-printed microfluidic devices. In particular, the modular nature of 3D-printed microfluidics offers significant potential for large-scale droplet production by interconnecting multiple units, and the surface treatment strategy presented here is expected to play a crucial role in ensuring stable and reliable operation under such high-throughput conditions.

Author contributions

G. Y., S. S., S. C., J. L., and R. S. designed the research. G. Y. and S. S. fabricated the devices and conducted the experiments. G. Y., J. L., and R. S. analyzed the data and prepared the manuscript. J. L. and R. S. supervised the work and edited the manuscript.

Conflicts of interest

There are no conflicts to declare.

Data availability

The data that support the findings of this study are available from the corresponding author upon reasonable request.

Acknowledgements

This research was supported by the Bio & Medical Technology Development Program of the National Research Foundation (NRF) funded by the Korean Ministry of Science and ICT (MSIT) (RS-2025-02305366), by the Basic Science Research Program through the NRF funded by the Ministry of Education (RS-2021-NR060123) and by the NRF grant funded by the MSIT (RS-2025-00516439 and RS-2025-16070978).

References

1 A. C. Bisen, S. Srivastava, A. Mishra, S. N. Sanap, A. Biswas, A. D. Choudhury, A. Dubey, N. M. Gupta, K. S. Yadav, M. N. Mugale and R. S. Bhatta, *J. Ocul. Pharmacol. Ther.*, 2024, **40**, 261–280.
2 N. Sadurni, C. Solans, N. Azemar and M. J. Garcia-Celma, *Eur. J. Pharm. Sci.*, 2005, **26**, 438–445.
3 L. M. Verissimo, L. F. A. Lima, L. C. M. Egito, A. G. de Oliveira and E. S. T. do Egito, *J. Drug Targeting*, 2010, **18**, 333–342.
4 K.-M. Kim, H. M. Oh and J. H. Lee, *Korean-Aust. Rheol. J.*, 2020, **32**, 243–249.
5 D. Venkataramani, A. Tsulaia and S. Amin, *Adv. Colloid Interface Sci.*, 2020, **283**, 102234.
6 C. C. Berton-Carabin, L. Sagis and K. Schroen, *Annu. Rev. Food Sci. Technol.*, 2018, **9**, 551–587.
7 M. Corredig and M. Alexander, *Trends Food Sci. Technol.*, 2008, **19**, 67–75.
8 B. Ozturk and D. J. McClements, *Curr. Opin. Food Sci.*, 2016, **7**, 1–6.
9 R. Zhang, W. Wu, Z. Zhang, Y. Park, L. He, B. Xing and D. J. McClements, *J. Agric. Food Chem.*, 2017, **65**, 9128–9138.
10 M. A. Mudassir, H. Z. Aslam, T. M. Ansari, H. Zhang and I. Hussain, *Adv. Sci.*, 2021, **8**, e2102540.

11 R. Song, S. Cho, S. Shin, H. Kim and J. Lee, *Nanoscale Adv.*, 2021, **3**, 3395–3416.
12 R. M. Erb, D. Obrist, P. W. Chen, J. Studer and A. R. Studart, *Soft Matter*, 2011, **7**, 8757–8761.
13 S. A. Nabavi, G. T. Vladisavljević, M. V. Bandulasena, O. Arjmandi-Tash and V. Manović, *J. Colloid Interface Sci.*, 2017, **505**, 315–324.
14 S. A. Nabavi, G. T. Vladisavljević, S. Gu and E. E. Ekanem, *Chem. Eng. Sci.*, 2015, **130**, 183–196.
15 A. S. Utada, E. Lorenceau, D. R. Link, P. D. Kaplan, H. A. Stone and D. Weitz, *Science*, 2005, **308**, 537–541.
16 T. Fujii, *Microelectron. Eng.*, 2002, **61–62**, 907–914.
17 G. G. Morbioli, N. C. Speller and A. M. Stockton, *Anal. Chim. Acta*, 2020, **1135**, 150–174.
18 S. K. Sia and G. M. Whitesides, *Electrophoresis*, 2003, **24**, 3563–3576.
19 I. D. Johnston, D. K. McCluskey, C. K. Tan and M. C. Tracey, *J. Micromech. Microeng.*, 2014, **24**, 035017.
20 C. Park, W. Lim, R. Song, J. Han, D. You, S. Kim, J. E. Lee, D. van Noort, C.-F. Mandenius and J. Lee, *Analyst*, 2024, **149**, 4496–4505.
21 Z. Wang, A. A. Volinsky and N. D. Gallant, *J. Appl. Polym. Sci.*, 2014, **131**, 41050.
22 G. Axel, G. Matthias and F. Henning, *J. Micromech. Microeng.*, 2001, **11**, 257.
23 S. C. Kim, D. J. Sukovich and A. R. Abate, *Lab Chip*, 2015, **15**, 3163–3169.
24 S. Bashir, M. Bashir, X. C. I. Solvas, J. M. Rees and W. B. Zimmerman, *Micromachines*, 2015, **6**, 1445–1458.
25 T. Trantidou, Y. Elani, E. Parsons and O. Ces, *Microsyst. Nanoeng.*, 2017, **3**, 1–9.
26 A. R. Abate, J. Thiele, M. Weinhart and D. A. Weitz, *Lab Chip*, 2010, **10**, 1774–1776.
27 A. R. Abate, D. Lee, T. Do, C. Holtze and D. A. Weitz, *Lab Chip*, 2008, **8**, 516–518.
28 R. Song, M. S. Abbasi and J. Lee, *Microfluid. Nanofluid.*, 2019, **23**, 1–11.
29 A. V. Nielsen, M. J. Beauchamp, G. P. Nordin and A. T. Woolley, *Annu. Rev. Anal. Chem.*, 2020, **13**, 45–65.
30 J. M. Zhang, A. A. Aguirre-Pablo, E. Q. Li, U. Buttner and S. T. Thoroddsen, *RSC Adv.*, 2016, **6**, 81120–81129.
31 S. Shin, S. Cho, R. Song, H. Kim and J. Lee, *Chem. Eng. J.*, 2023, **471**, 144734.
32 Q. Ji, J. M. Zhang, Y. Liu, X. Li, P. Lv, D. Jin and H. Duan, *Sci. Rep.*, 2018, **8**, 1–11.
33 T. Kawakatsu, G. Trägårdh, C. Trägårdh, M. Nakajima, N. Oda and T. Yonemoto, *Colloids Surf., A*, 2001, **179**, 29–37.
34 R. Landgraf, M.-K. Kaiser, J. Posseckardt, B. Adolphi and W.-J. Fischer, *Procedia Chem.*, 2009, **1**, 1015–1018.
35 Y.-H. Hwang, T. Um, G.-N. Ahn, D.-P. Kim and H. Lee, *Chem. Eng. J.*, 2022, **431**, 133998.
36 T.-H. Yoon, M. Li, L.-Y. Hong, J. Lee and D.-P. Kim, *Anal. Chem.*, 2011, **83**, 1901–1907.
37 M. J. Männel, N. Weigel, N. Hauck, T. Heida and J. Thiele, *Adv. Mater. Technol.*, 2021, **6**, 2100094.
38 T. W. Bacha, D. C. Manuguerra, R. A. Marano and J. F. Stanzione, *RSC Adv.*, 2021, **11**, 21745–21753.
39 B. Rånby, W. T. Yang and O. Tretinnikov, *Nucl. Instrum. Methods Phys. Res., Sect. B*, 1999, **151**, 301–305.
40 K. Studer, C. Decker, E. Beck and R. Schwalm, *Prog. Org. Coat.*, 2003, **48**, 92–100.
41 G. Li, G. He, Y. Zheng, X. Wang and H. Wang, *J. Appl. Polym. Sci.*, 2012, **123**, 1951–1959.
42 T. Segers, L. De Rond, N. De Jong, M. Borden and M. Versluis, *Langmuir*, 2016, **32**, 3937–3944.
43 B. van Elburg, G. Collado-Lara, G.-W. Bruggert, T. Segers, M. Versluis and G. Lajoinie, *Rev. Sci. Instrum.*, 2021, **92**, 3.
44 O. Tretinnikov, V. Pilipenko and L. Prikhodchenko, *Polym. Sci., Ser. B*, 2012, **54**, 427–433.
45 C. Decker and A. D. Jenkins, *Macromolecules*, 1985, **18**, 1241–1244.
46 O. Tretinnikov, V. Pilipenko and L. Prikhodchenko, *Polym. Sci., Ser. B*, 2012, **54**, 427–433.
47 M. S. Bell and A. Borhan, *ACS Omega*, 2020, **5**, 8875–8884.
48 J. Wu, J. Lin, G. Li and C. Wei, *Polym. Int.*, 2001, **50**, 1050–1053.
49 A. Kamnerdsook, E. Juntasaro, N. Khemthongcharoen, M. Chanasakulniyom, W. Sripumkhai, P. Pattamang, C. Promptmas, N. Atthi and W. Jeamsaksiri, *Colloids Interfaces*, 2023, **7**, 17.
50 P. Zhu and L. Wang, *Lab Chip*, 2017, **17**, 34–75.
51 S. Cleve, A. Lassus, C. Diddens, B. Van Elburg, E. Gaud, S. Cherkaoui, M. Versluis, T. Segers and G. Lajoinie, *J. Fluid Mech.*, 2023, **972**, A27.
52 B. Riechers, F. Maes, E. Akoury, B. Semin, P. Gruner and J.-C. Baret, *Proc. Natl. Acad. Sci. U. S. A.*, 2016, **113**, 11465–11470.

